Tunable Assembly of Colloidal Crystal Alloys Using Magnetic Nanoparticle Fluids

Ye Yang,[†,§] Lu Gao,[†,§] Gabriel P. Lopez,[†,‡,§] and Benjamin B. Yellen[†,§,⊥,*]

[†]Department of Mechanical Engineering and Materials Science and [‡]Department of Biomedical Engineering, Duke University, Durham, North Carolina 27708, United States, [§]Research Triangle Materials Research Science and Engineering Center, North Carolina, United States, and [⊥]University of Michigan-Shanghai Jiao Tong University—Joint Institute, Shanghai, People's Republic of China

ABSTRACT We demonstrate a magnetic technique for assembling bidisperse and tridisperse colloidal particle fluids into a variety of complex structures with dimensionality ranging from 0-D (rings) to 1-D (chains) to 2-D (tiles). Compared with prior work on bidisperse particles that are commensurate in size, here we explore the assembly of different sized particles, and we show that due to packing constraints, new particle structures can be realized experimentally. Extending these experiments to a tridisperse system, we demonstrate that at low concentrations the smallest particle does not change the underlying crystal structures of the bidisperse system; however, it can assist in the formation of crystallite structures that were not stable in a bidisperse system. Additionally, we discovered that the smallest particle mimics the role of the ferrofluid, by shifting the locations in phase space where the bidisperse crystal structures can be experimentally obtained. Finally, we demonstrate that 3-particle crystal structures can be tuned by varying the strength of the external field, which is not possible in a 2-particle system.

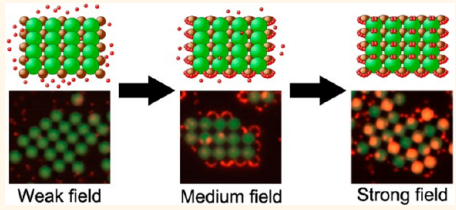

KEYWORDS: magnetic assembly · colloidal particles · ferrofluid · paramagnetic · diamagnetic · dipole—dipole interaction · tunable

The structural diversity of natural crystalline materials, which lead to their myriad of electrical, mechanical, magnetic, and chemical properties, has inspired intense efforts to build artificial crystalline materials to achieve similar properties in engineered devices. Recent work has demonstrated the vast range in functionality of artificial crystals, such as in the development of photonic[1−5] and phononic bandgaps,[6−8] and their use in electromagnetic and acoustic cloaking,[9−11] as well as their ability to achieve optical,[12,13] thermal,[14,15] and acoustic[16,17] rectification. In many of these examples, "top-down" fabrication methods based on photolithography, mechanical molding, and direct printing, have been successfully applied to fabricate artificial crystalline materials that can operate in the long wavelength regime, for example, the microwave and infrared regime.[18,19] Scaling these materials to operate at shorter wavelengths, such as the visible regime, however, has been more challenging due to the strict requirements on the size and crystal structure of the unit cell.[20,21] While photolithography has been successfully used to create photonic crystal devices in the near-infrared range,[22−25] it remains a formidable challenge to fabricate multilayer 3D structures that can eventually be adopted by industry.

"Bottom-up" fabrication techniques based on self-assembly are currently being investigated as an alternative approach for fabricating artificial crystalline materials.[26,27] Self-assembled colloidal crystalline materials have received significant attention in recent years because of their ability to build crystal structures with length scales suitable for controlling visible light.[28,29] Self-assembly techniques have greatly benefited from recent advances in chemistry and materials science, which can synthesize monodisperse colloidal micro- and nanoparticles from a wide variety of precursors. Self-assembly has the additional advantage of permitting the construction of 3-D structures[30−32] and can be built on both planar and nonplanar surfaces.[33,34] However, self-assembled crystals are prone to defects and are usually restricted to a limited number of crystalline structures, which limit potential applications.

Recently, there has been increasing interest in extending these self-assembly principles to build "colloidal alloys" in which two or more types of colloidal particles are arranged into well-defined crystalline configurations. Techniques based on controlled

* Address correspondence to yellen@duke.edu.

Received for review January 9, 2013 and accepted February 1, 2013.

Published online February 01, 2013
10.1021/nn400118e

drying,[35−37] ionic interactions,[38−40] and molecular recognition,[41−45] as well as electric and magnetic fields,[46−49] have demonstrated a variety of new crystal structures that cannot be produced in monocomponent suspensions. However, the ability to assemble large colloidal crystal structures and methods to precisely control the crystallinity remain a fundamental challenge.

Of all the above-mentioned colloidal assembly techniques, field-assisted assembly methods are unique in their ability to control the particle−particle interactions in real-time.[46−59] There are many examples of field-assisted assembly of monodisperse colloidal suspensions,[50−53,55,58,59] and more recently there have been some examples of colloidal structures assembled from bidisperse and tridisperse colloidal suspensions.[46−49] Here, we extend these early investigations and demonstrate a wide class of tile, chain, and ring structures that can be assembled in 2- and 3-particle systems, in which the particles have both different sizes and different material properties. Additionally, we demonstrate that the strength of the applied magnetic field can induce phase transitions in a 3-particle system, which cannot be observed in a 2-particle system.

Our system consists of a suspension of spherical, isotropic magnetic, and nonmagnetic colloidal particles of different sizes, which are immersed in a suspension of magnetic nanoparticles, known as ferrofluid. Here, the ferrofluid nanoparticles are much smaller than the other colloidal particles and thus can be treated as a magnetic continuum, whose properties can be tuned by controlling the magnetic nanoparticle concentration. Colloidal particles with a magnetic permeability that is higher than the ferrofluid exhibit a paramagnetic response, in which the effective dipole moment of the particle aligns parallel to the external field. Colloidal particles with a magnetic permeability that is lower than the ferrofluid exhibit a diamagnetic response, in which their moments align antiparallel to the external field. The resulting attractive and repulsive interactions both between similar particles and dissimilar particles vary as a function of their relative magnetic permeabilities, relative concentrations, and relative positions with respect to the external field direction. Subtle tuning of these interactions allows for a diverse array of colloidal structures to be assembled. Our experiments are guided by a relatively simple theoretical model based on the summation of dipole−dipole interactions between the particles, which allows for minimum energy configurations to be determined as a function of several control parameters.

In this work, we first analyze the type of structures that can be assembled in a 2-particle system (one magnetic and one nonmagnetic bead type) as a function of the ferrofluid concentration and relative particle concentration. We demonstrate that much of the assembly process can be described by finding the lowest potential energy structure of different lattice configurations; however, we also observed that kinetic effects and entropic effects can play a role in the assembly process. Next, we analyze the structures assembling in a 3-particle system (one magnetic and two nonmagnetic bead types), and we demonstrate that the external field strength can induce phase transitions between different colloidal structures. To our knowledge, this is the first demonstration of a field-induced phase transition in a multicomponent colloidal suspension.

THEORY AND NOTATION

Spherical, linearly magnetizable particles immersed in a homogeneous fluid and exposed to an external uniform field are reasonably approximated as a collection of magnetic point dipoles.[48] The strength of interaction between the point dipoles is a function of the relative dipole orientations and their relative positions. In these experiments, colloidal particles are confined to a thin fluid film, in which the external field is applied normal to the film surface. The large (4.8 μm) and medium (2.7 μm) sized beads are typically confined to a 2-D plane, in which the pairwise particle−particle interaction energy is given as the scalar product:

$$U_{ij} = \frac{\mu_f}{4\pi}\frac{m_i m_j}{{r_{ij}}^3} \quad (1)$$

where μ_f is the magnetic permeability of the ferrofluid, and m_i and m_j are the dipole moments of the two particles i and j, which are separated by a distance r_{ij} within the 2-D plane. This expression is similar to that for electrostatic interactions, except that it follows r^{-3} instead of r^{-1} dependence. In cases where a third small (1-μm) bead is also present, it is typically located either within the 2-D plane, and follows the energetics of eq 1, or directly on top of other particles, in which the energetics follows the same scaling relationship except for multiplication by a factor of negative two.

The effective dipole moments of the particles depend on the magnetic permeability mismatch with respect to the surrounding medium as well as the local field, which can be expressed as

$$\vec{m}_i = 3\left(\frac{\mu_i - \mu_f}{\mu_i + 2\mu_f}\right)V_i\vec{H}_i = \bar{\chi}_i V_i \vec{H}_i \quad (2)$$

where μ_i is the magnetic permeability of the ith particle type having volume V_i and experiencing a magnetic field H_i at the particle's center, while μ_f is the ferrofluid permeability. Since the magnetic nanoparticles comprising the ferrofluid are orders of magnitude smaller than the other colloidal particles, the ferrofluid is treated as a homogeneous medium with a magnetic permeability of $\mu_f = \mu_0(1 + \varphi\chi_B)$, where χ_B is the bulk susceptibility of ferrofluid, and φ is the volume fraction of solids within the ferrofluid. In our experimental system, the nonmagnetic particles denoted by subscript

n have permeabilities roughly equal to that of vacuum, *i.e.*, $\mu_n \approx \mu_0 < \mu_f$, or using the short-hand notation, $\bar{\chi}_n < 0$. The magnetic particles denoted by subscript m typically have a magnetic permeability greater than the ferrofluid, that is, $\mu_m > \mu_f$, or using the short-hand notation, $\bar{\chi}_m > 0$. Thus the interaction between these positive and negative dipoles leads to antiferromagnetic interactions within the 2-D plane and ferromagnetic interactions along the field direction. In the computation of phase diagrams, we restrict our attention to the 2-particle system, in which all particles are confined to the 2-D plane. Thus, the potential energy of a given crystalline configuration is determined by summing the interactions of all particles, given by

$$U = \sum_{i=1}^{N} \sum_{j=i+1}^{N} \frac{m_i m_j}{4\pi d_{ij}^3} \tag{3}$$

and the energy per particle is given by

$$u = \frac{U}{N} \tag{4}$$

where *N* is the total number of particles (in the limit taken to infinity). For sufficiently large size lattice, the summation will lead to a convergent value of *u*. In our calculation of 1D and 2D structures, we maintained a sufficiently large particle number ($N > 10000$ in the calculation) such that convergence of the energy density to within 1% accuracy could be achieved.

A simplifying assumption was used to allow the particle number ratio, N_n/N_m, affect the total system energy. Specifically, we assumed that the interaction energy of the entire system was produced by particles that are incorporated into a particular lattice structure as well as any leftover free particles. These free particles were assumed to be sufficiently far away from the other structures that they produce a negligible effect on the energy density of a particular lattice; however, their presence does affect the system energy density. In experiments, the free particles were typically several diameters away from other structures, which justifies this assumption.

In calculating the system energy, we used a parameter *k* to define the particle number ratio:

$$k = \frac{N_n}{N_m} \tag{5}$$

whereas the parameter *s* represent particle stoichiometry for a given crystal structure:

$$s = \frac{N_n^*}{N_m^*} \tag{6}$$

When the particle number ratio is higher than the crystal stoichiometry ($k > s$), there will be an excess of nonmagnetic particles, and the structure in the system is limited by magnetic particles. In this case, the average energy density of the system is

$$u_s = \frac{1+s}{1+k} u \tag{7}$$

where *u* is the energy density of an infinite lattice defined in eq 4. Similarly, when the particle number ratio is lower than the crystal stoichiometry ($k < s$), there is an excess of nonmagnetic particles and the average energy density is given by

$$u_s = \frac{1+s^{-1}}{1+k^{-1}} u \tag{8}$$

Through this approach, we evaluated the system energy density of the 26 structures observed in experiments (including several crystallites), and constructed a $T = 0$ free energy phase diagram by selecting the structure which had the lowest system energy as a function of the ferrofluid concentration and particle number ratio. We recognize that entropy can play an important role in the total free energy of different phases, especially for dense colloidal particle suspensions; however, it is an enormous computational challenge to introduce entropy into these calculations, which typically rely on some type of molecular dynamics or Monte Carlo type calculation, and still compute the large parameter space necessary to produce a phase diagram. Thus, the calculations presented here should be treated more as a guide to determining the experimental conditions in which different colloidal structures can assemble.

More than 20 different colloidal crystal structures were observed in experiments, thus for simplicity, we used the notation M_xN_y to refer to the stoichiometry of a structure in which a unit cell contains *x* paramagnetic particles and *y* diamagnetic particles.

RESULTS AND DISCUSSION

2-Particle Assembly System. In contrast with prior studies on the magnetic assembly of binary colloidal lattices, which focused on two particle types that are commensurate in size,[48] here we explore the magnetic assembly of 4.8-μm nonmagnetic particles and 2.7-μm magnetic particles with a diameter ratio of ~1.7. We show that several new lattice structures become stable for this size ratio, whereas other lattice structures become unstable, which is due to differences in how particles can pack into different 2-D crystal structures.[62−64]

The two main examples of tile structures observed in experiments are shown in Figure 1. These tile structures, which include MN square lattice (Figure 1a) and M_2N honeycomb lattices (Figure 1b), are significantly larger than in prior work,[48] due to the use of acoustic field to locally concentrate the particles before the magnetic assembly process (see Supporting Information Figure S2). Tile structures form when the ratio of the particle dipole moments is inversely proportional

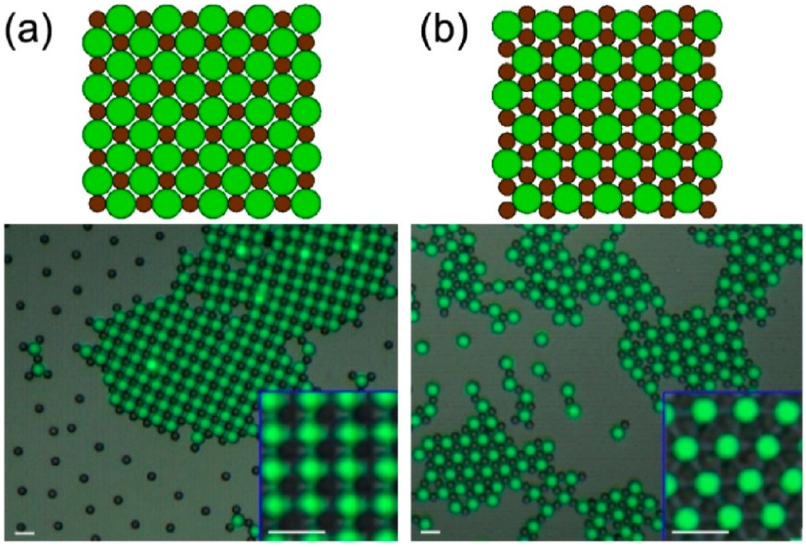

Figure 1. 2D tile structures can be observed at different ferrofluid concentrations, including (a) MN square lattice for $\varphi = 0.5\%$ and (b) M_2N honeycomb lattice for $\varphi = 0.8\%$. Brightfield and fluorescent images are overlaid to increase the image contrast. Illustrations are provided above each experimental image, where the nonmagnetic particles are green and magnetic particles are dark brown. The tile structures were assembled in an external field of 15 Oe. The scale bars are 10 μm.

to their relative population fraction within the unit cell, leading to a unit cell structure with nearly zero net dipole density. The largest single-crystal MN square lattices were observed to form in a ferrofluid concentration of ~0.5% vol. fraction of magnetic nanoparticles and when the relative particle concentrations were roughly equal, having the assembly conditions $\bar{\chi}_n V_n/\bar{\chi}_m V_m \approx -1$ and $N_m/N_n \approx 1$. The largest single-crystal M_2N honeycomb lattices were observed in a ferrofluid concentration of ~0.8% vol. fraction of magnetic nanoparticles and when the magnetic particle concentration was twice that of the nonmagnetic particle concentration, having the assembly conditions $\bar{\chi}_n V_n/\bar{\chi}_m V_m \approx -2$ and $N_m/N_n \approx 2$. A large field of view images for different colloidal phases are provided in the Supporting Information (see Figure S3).

In contrast with prior results on the assembly of commensurately sized particles,[48] here we observed that the MN square lattice formed the largest tile structures as opposed to the M_2N honeycomb and M_3N kagome lattices. This difference can be attributed to the denser packing fraction for square lattice at this particle size ratio (the 2-D packing fraction is 0.85 for the square lattice, 0.8 for the honeycomb lattice, and 0.72 for the kagome lattice with a particle size ratio of 1.7), which both favors the depletion interaction between particles and has higher entropy.[60,61] We only observed small fragments of kagome lattices in this system for two reasons: (1) the kagome lattice is the least densely packed and (2) the ferrofluid concentrations required to achieve kagome lattice was >1%, which is difficult to obtain in our experimental system.

When the net dipole density of the unit cell diverges from zero, the dipole−dipole interaction between unit cells introduces strain within the crystal, and causes the tiles to break up into 1-D chain structures. Figure 2 shows the four types of chain structures that were observed in experiments, including MN_2 chains (Figure 2a), MN chains (Figure 2b), M_2N_2 chains (Figure 2c) and M_2N chains (Figure 2d). Compared with systems of commensurately sized particles, we note several differences. First, the MN_5 and MN_4 chains were not present in this system due to packing constraints. Second, we observed the presence of the M_2N_2 chain, which was not frequently observed in the system of commensurately sized particles. Finally, we noticed that the MN chains were more stable in this system and were commonly found for a variety of experimental conditions. At the boundary between experimental conditions that favor chain *vs* tile phases, we sometimes observed a mixed phase that resembled a percolating network of chains (see Supporting Information Figure S4).

Owing to the intricate balance between the repulsive and attractive interactions between the particles and the loose packing of the 1-D chain structures, the bond angles for particles within the M_2N and M_2N_2 chains could be adjusted with the ferrofluid concentration. At ferrofluid concentrations of 0.5%, for example, the magnetic beads experience greater repulsion than the nonmagnetic beads, leading to bond angles of 99° and 92° for the M_2N, and M_2N_2 chains, respectively. Conversely, at ferrofluid concentrations of 0.8% the nonmagnetic beads experience greater repulsion than the magnetic beads, leading to bond angles of 118° and 82° for the M_2N, and M_2N_2 chains, respectively (see Supporting Information Figure S3). For the sake of convenience, in the illustrations we depict the M_2N and M_2N_2 chains with a 90° bond purely, regardless of the actual bond angle observed in a given experiment.

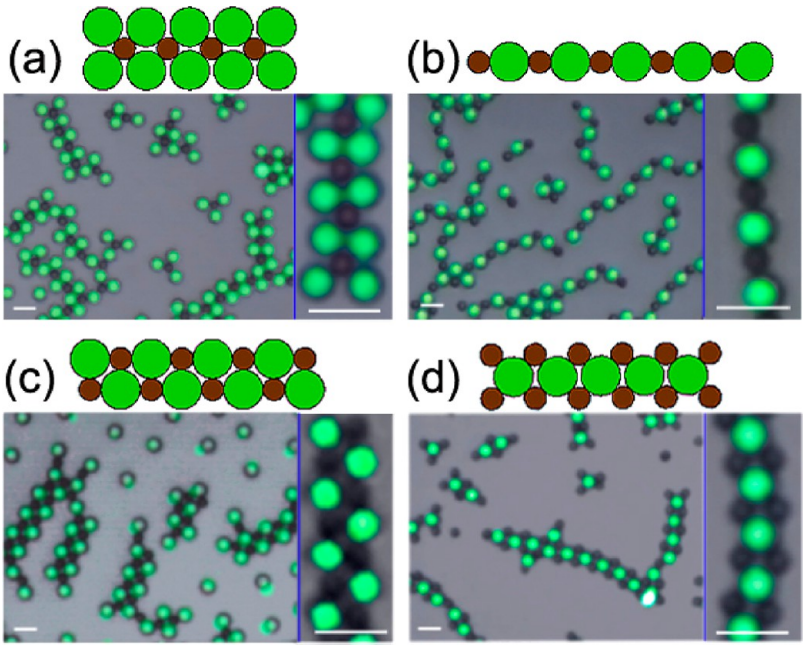

Figure 2. 1D chain structures were observed at the ferrofluid concentrations of (a) MN_2 chain for φ = 0.2%; (b) MN chain for φ = 0.3%; (c) M_2N_2 chain for φ = 0.7%; and (d) M_2N chain for φ = 0.8%. Brightfield and fluorescent images are overlaid to increase the image contrast. Illustrations are provided for each structure where the nonmagnetic particles are green and magnetic particles are dark brown. The tile structures were assembled in an external field of 15 Oe. The scale bars are 10 μm.

When the dipole density of the unit cell strongly diverges from zero, both the tile and chain phases are energetically unstable, and instead ring structures tend to assemble. Figure 3 shows the transition between different ring structures as a function of increasing ferrofluid concentration. In addition to the ring structures, we observed the formation of several crystallite structures which express 5-fold or 3-fold symmetry that could be reliably obtained at certain experimental conditions (see Figure 3k−m).

Figure 4 presents the 2-particle phase diagram, which was constructed by determining the lowest system energy configuration eq 1−8 among the 26 lattice structures as a function of the ferrofluid and relative particle concentrations. In all the calculations, we assumed the magnetic susceptibility was $\chi_m = 0.45$ for the magnetic particles, and $\chi_n = 0$ for nonmagnetic particles, which is consistent with the materials data sheet provided by the manufacturer. The susceptibility of the ferrofluid is assume to follow a linear relationship with the particle concentration as $\chi_f = \chi_B\varphi$, where φ is the ferrofluid volume fraction, and χ_B is the susceptibility of bulk iron-oxide nanoparticles, whose best fit was determined to be 14.2.

In calculating the system energy for the chain structures, we did not allow for continuously varying bond angles for M_2N_2 and M_2N chains, and instead assumed that the bond angles were fixed at 90°. The system energy calculated for the two bond angles of the M_2N chains (90° and 120°) had relatively small energy variations, which justifies this simplification. In practice, this assumption led to minor movement of the phase boundaries bordering the M_2N_2 and M_2N chain phases; however, the effect is small.

In calculating the magnetic moments of the beads, we did not explicitly include the nearest neighbor interaction like in previous work.[48] We note that when we did consider nearest neighbor interactions (data not shown) it had only a minor effect on the phase diagram by shifting certain phase boundaries.

In many respects theory and experiment match quite well, whereas in other respects they match poorly. For example, the phase diagram correctly predicts the experimental locations of the tile structures (square data points are tightly grouped in the correct locations). The experimental locations of the ring structures are correctly predicted to exist near the extremities of the phase diagram. The MN_2 chains (green + signs are tightly grouped), the M_2N_2 chains (orange + signs are tightly grouped in two spots), the M_2N chains (one of the groupings of red crosses), and the MN chains (one of the groupings of the blue crosses) were observed in the vicinity of the theoretically predicted locations. The M_5N_6 5-fold symmetry crystallite (green stars) were also observed near the predicted locations.

There are several examples where theory and experiment do not match. For example, the M_4N_3 crystallite expressing 3-fold symmetry was never predicted to be the lowest energy phase, though it was observed experimentally at the border between the MN square lattice and M_2N honeycomb lattices. Likewise, the M_3N_3 crystallite was never predicted to be the lowest energy phase, though it was observed near the border between the MN chain and M_2N ring phases. Neither of

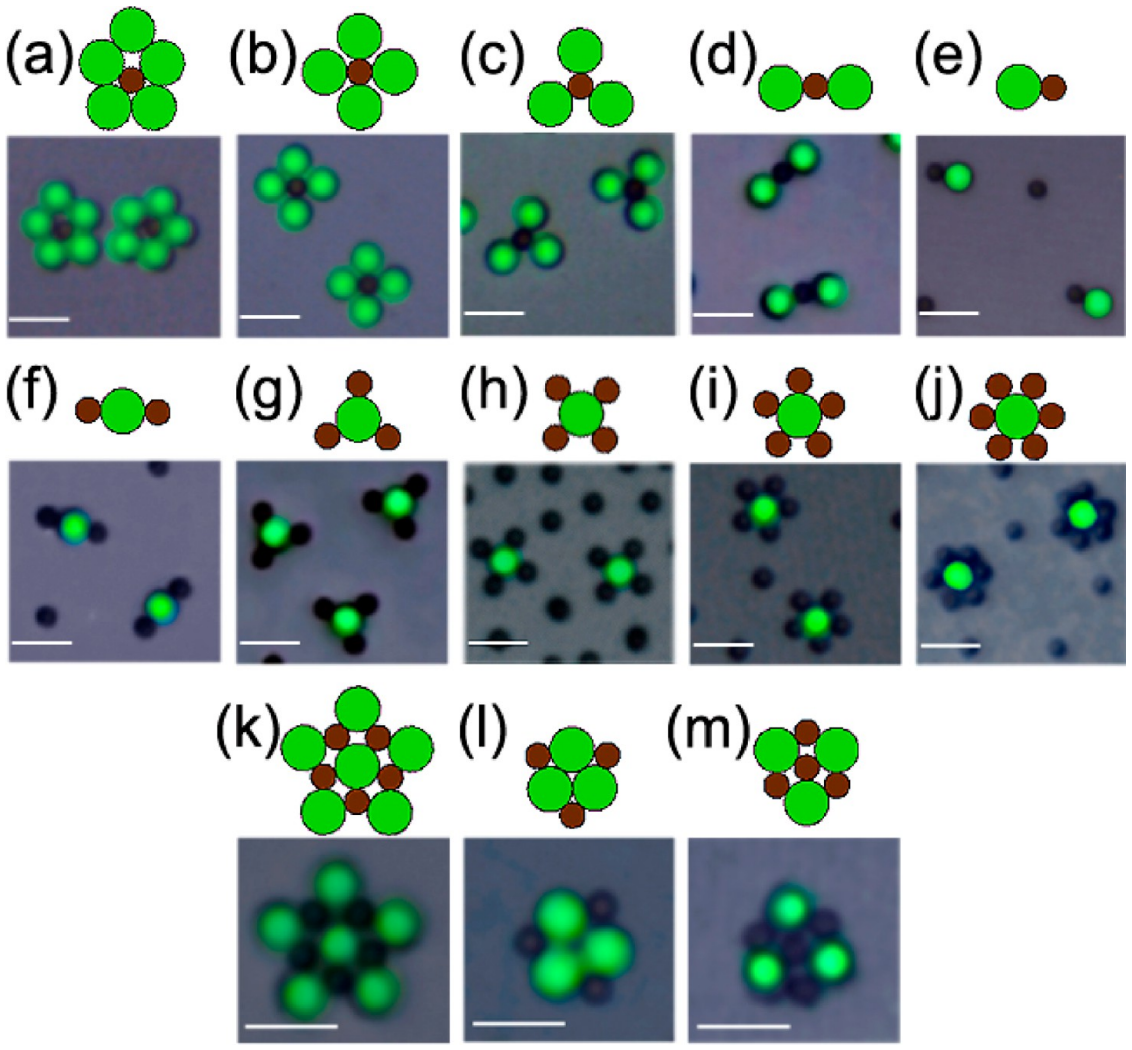

Figure 3. 0D ring structures were observed at ferrofluid concentrations of (a) MN_5 for $\varphi = 0.1\%$, $N_m/N_n = 0.2$; (b) MN_4 for $\varphi = 0.1\%-0.2\%$, $N_m/N_n = 0.25$; (c) MN_3 for $\varphi = 0.2\%-0.4\%$, $N_m/N_n = 0.3$; (d) MN_2 for $\varphi = 0.3\%-0.5\%$, $N_m/N_n = 0.5$; (e) MN for $\varphi = 0.1\%-0.2\%$, $N_m/N_n = 1$; (f) M_2N for $\varphi = 0.2\%$, $N_m/N_n = 2$; (g) M_3N for $\varphi = 0.3\%-0.5\%$, $N_m/N_n = 3$; (h) M_4N for $\varphi = 0.6\%-0.8\%$, $N_m/N_n = 4$; (i) M_5N for $\varphi = 0.9\%$, $N_m/N_n = 5$; (j) M_6N for $\varphi = 1.0\%$, $N_m/N_n = 6$. We also observed several types of crystallites, including (k) M_5N_6 crystallite with 5-fold symmetry for $\varphi = 0.7\%-0.8\%$; (l) M_3N_3 crystallite with 3-fold symmetry for $\varphi = 0.1\%-0.2\%$, and (m) M_4N_3 crystallite with 3-fold symmetry for $\varphi = 0.6\%-0.7\%$. Illustrations are provided for each structure where the nonmagnetic particles are green and magnetic particles are dark brown. The tile structures were assembled in an external field of 15 Oe. The scale bars are 10 μm.

these cases is that surprising because the energy difference between these configurations compared with the lowest energy state was on the order of thermal energy.

We also found that the MN chains were often observed in coexistence with the MN square lattice phase, and likewise the M_2N chain structures were observed in coexistence with the M_2N honeycomb lattices. These discrepancies are also not surprising, since there was only a small potential energy difference between the chain and tile structures for a variety of experimental conditions.

The most striking example where theory and experiment diverge is for the conditions $N_n/N_m > 2$ and $0.3\% < \varphi < 1.0\%$, in which ring structures were predominantly observed in experiments whereas chain structures were theoretically predicted. The disagreement between theory and experiment may be caused by kinetic limitations in the assembly process, and thus provide some hints for how the dynamics of the assembly process may evolve. For the conditions $N_n/N_m > 2$ and $\varphi = 0.4\%$, as one example, the MN_2 chain structure is predicted to have the lowest energy state; however, a mixture of MN_2, MN_3, and MN_4 rings was typically observed. In experiments, the dynamics typically begin with the formation of ring structures, which later evolve into higher dimensional chains and tile structures. Depending on the strength of the external field, these metastable states can be long-lived (*e.g.*, escape time scales can be hours or longer for micrometer-sized particles).

However, another possible explanation for the divergence between theory and experiment is the lack of entropy in the energy calculations, which was omitted

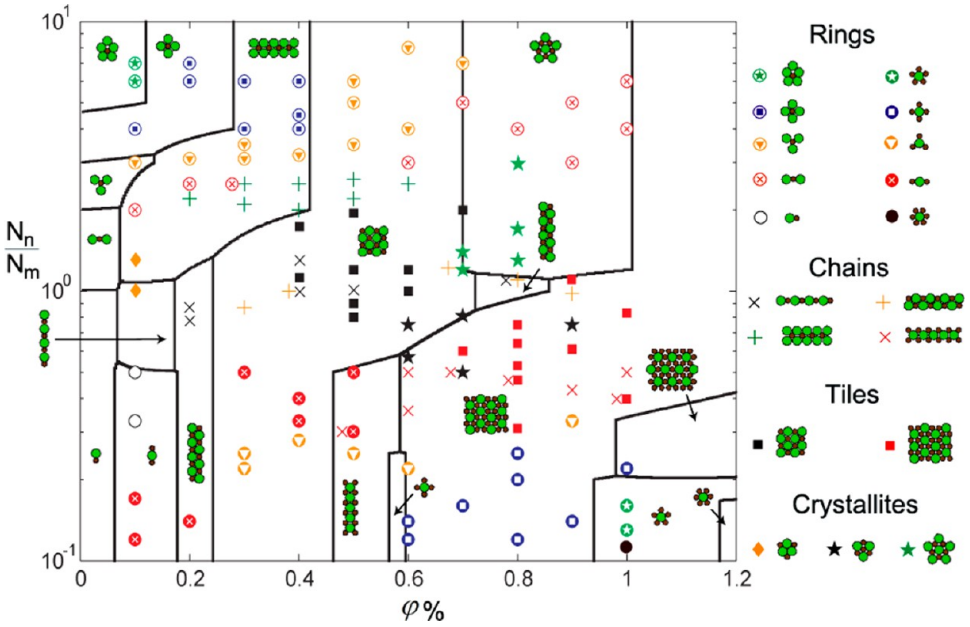

Figure 4. A $T = 0$ phase diagram is plotted by determining the minimum energy state among the 26 different lattice structures as a function of the ferrofluid and relative particle concentrations. Experimental data points for the ring (circles), chains (crosses), tiles (squares), and crystallites (diamonds and stars) are included.

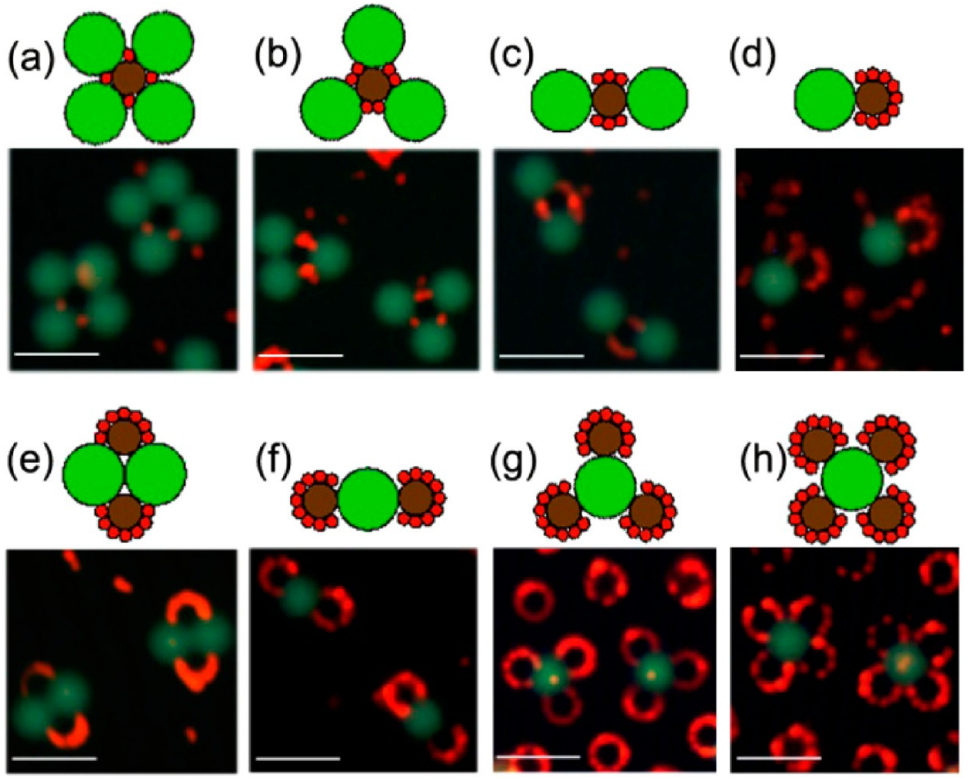

Figure 5. Hierarchical assembly of 3-particle ring strictures is illustrated on the underlying ring templates (a) MN_4 ring, which was observed for $\varphi = 0.1\%$, $N_L/N_M = 4$; (b) MN_3 ring, which was observed for $\varphi = 0.1\%-0.2\%$, $N_L/N_M = 3$; (c) MN_2 ring, which was observed for $\varphi = 0.1\%-0.2\%$, $N_L/N_M = 2$; (d) MN ring, which was observed for $\varphi = 0.1\%-0.2\%$, $N_L/N_M = 1$; (e) M_2N_2 crystallite, which was observed for $\varphi = 0.2\%-0.3\%$, $N_L/N_M = 1$; (f) M_2N ring, which was observed for $\varphi = 0.1\%-0.2\%$, $N_L/N_M = 2$; (g) M_3N ring, which was observed for $\varphi = 0.3\%-0.4\%$, $N_L/N_M = 3$; and (h) M_4N ring, which was observed for $\varphi = 0.4\%$, $N_L/N_M > 4$. The illustrations depict the crystal structures, in which the 1 μm particles (S) are red, 2.7 μm particles (M) are dark brown, and 4.8 μm particles (L) are green. The scale bars are 10 μm.

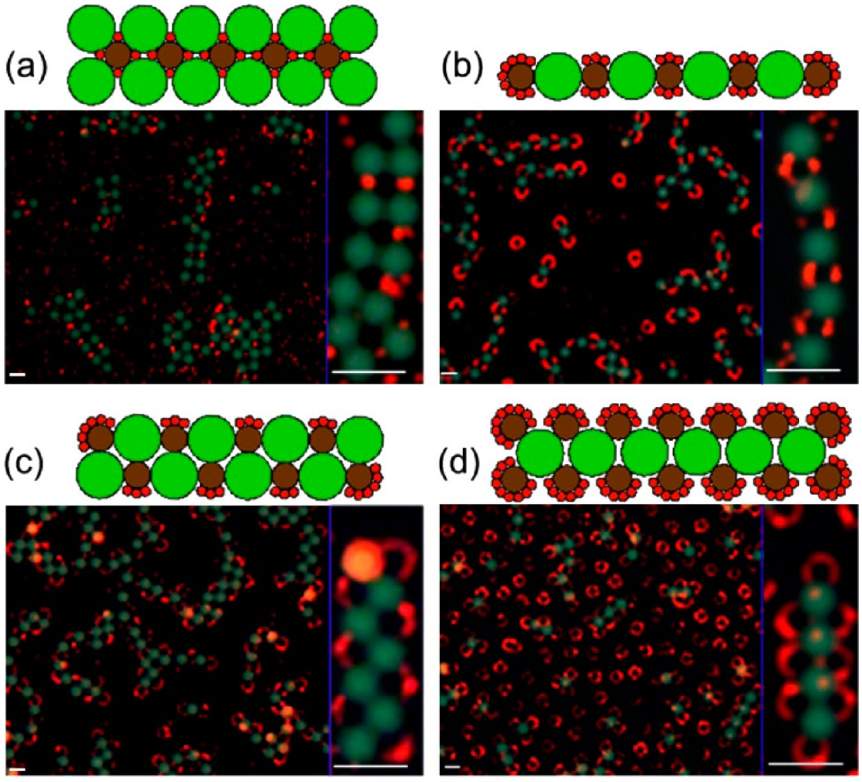

Figure 6. Assembly of chain superstructures, such as (a) MN_2 chain; (b) MN chain; (c) M_2N_2 chain; (d) M_2N chain. Those structures also have two levels of complexity: the first level is similar to chain structures in 2-particle, and the second level as "Saturn Rings" formed by 1 μm particles packing against 2.7 μm magnetic particles. Illustrations are provided for each structure, in which the 1 μm particles (S) are red, 2.7 μm particles (M) are dark brown, and 4.8 μm particles (L) are green. All the scale bars are 10 μm.

due to the computational difficulty in modeling the entropy of large particle systems which typically require a Monte Carlo[62,63] or molecular dynamics simulation.[64,65] Since the energy of a collection of multiple ring structures is higher than the entropy of a single chain structure, this may represent another plausible explanation. Despite these minor discrepancies, the main conclusion is that the combination of theory and experiment allows a particular crystal structure to be assembled in a repeatable manner by carefully controlling the ferrofluid and relative particle concentrations.

3-Particle Assembly System. Building on the results from the 2-particle assembly system, we next explored a 3-particle assembly system by adding 1 μm nonmagnetic particles at concentrations that are equivalent to the 2.7 μm magnetic particles in terms of volume fraction. For convenience of notation, in the following discussion we will label the beads as L (large, nonmagnetic), M (medium, paramagnetic), and S (small, nonmagnetic). Because of their small size and low concentration, the S particles did not significantly alter the fundamental crystal structures of the 2-particle system. Instead, the S particles decorated the crystal structures by either forming rings around the M particles or clumps on top of the L particles. The relative abundance of the S particles at either location depends strongly on the ferrofluid concentration. For example, at low ferrofluid concentrations (φ < 0.3%) the magnetic permeabilities of the nonmagnetic beads were relatively weak, and thus the S particles interacted strongly with the M particles and weakly with the L particles. In this case, the S particles typically formed ring structures around the equator of the M particles. Alternatively, at high ferrofluid concentrations (φ > 0.4%), the magnetic permeabilities of the nonmagnetic particles were large compared to the magnetic particles, and thus the S particles interacted more strongly with the L particles, and typically formed clumps on top of the L particles.

The degree of incorporation of the S particles into the 2-particle crystalline templates also depends on the type of base 2-particle crystal structure. For crystal structures that have a relative abundance of the L particles, the accessibility for the S particles to assemble around equator of the M particles are restricted, presumably due to geometric constraints. Some of the S particles occupied the interstitial regions with the crystals, whereas the rest were randomly dispersed in the fluid. For crystal structures that have a relative abundance of the M particles, on the other hand, a large number of S particles could be incorporated into the crystal structures. This effect can be clearly observed in Figure 5, in which the red rings are particularly prominent for Figure 5c–h, for the underlying ring templates MN_2, MN, M_2N, M_3N, and M_4N, and crystallite template M_2N_2. By

contrast, few S particles could assemble into the ring templates MN_3 and MN_4, as shown in Figure 5a–b.

It is interesting to note that the addition of the S particles increased the stability of several structures that were not stable in a 2-particle system. For example, we rarely observed a stable M_2N_2 crystallite in the 2-particle system; however, in the 3-particle system this structure was commonly observed (see Figure 5e). The presence of these new structures may be due to the ability of the S particles to balance the net dipole moment of the overall structure. In a 2-particle system, the balancing process would promote the formation of large tile structures, such as the MN square lattice. In a 3-particle system, on the other hand, the S particles can act to shield the moment of the M particles, and thus balance the net dipole moment of the structure in a competitive manner.

Similar trends are observed for the hierarchical assembly of chain structures, shown in Figure 6. The S particles are incorporated to a greater extent in the underlying crystal templates when there is a relative abundance of the M particles (i.e., the MN, M_2N_2, M_2N chain structures of Figure 6b–d), whereas, relatively few S particles are incorporated into the MN_2 chain structure presumably due to geometric constraints (see Figure 6a).

In the 3-particle experiments, we limited the ferrofluid concentration to the range of 0.1% to 0.4%, in which the MN square lattice was the only tile structure observed for these conditions. In general, presumably due to packing constraints, the S particles were restricted from being incorporated in the interior of the crystal in large quantities. Instead, the S particles assembled around the periphery of the tile structures when the sides were terminated by the M particles (see Figure 7b).

Another interesting observation is that the type of assembled structure can be tuned by adjusting the field strength in this 3-particle system. In weak fields (~8 Oe), the interaction between the M and L particles is larger than thermal energy; however, the interaction between the S and M particles and the S and L particles is smaller than thermal energy. In this case, 2-particle lattices assemble in the fluid, meanwhile the S particles are randomly dispersed (Figure 7a). As the field is increased beyond a critical threshold (~20 Oe), the interaction between the S and M particles is higher than thermal energy, but the interaction between the S and L particle is still lower than thermal energy. In this case, a 3-particle crystal structure can assemble, such as the one shown in Figure 7b. When the field is further increased (beyond ~30 Oe), the interactions between M and L particles, S and M particles, and S and L particles are all larger than thermal energy, in which case the S particles can assemble both on top of the L particles and around the M particles, such as the crystal structure shown in Figure 7c.

Generally, these field-induced transitions depend on the relative concentrations of the S, M, and L, particles, and on the ferrofluid concentration. The field induced transition requires a sufficiently high concentration of the S particles, such that after saturating the surface sites near one particle type (say, around the M particles), the S particles next assemble around the other particle type when the interaction energy is larger than k_BT. In low ferrofluid concentrations (below 0.3%), the interaction between S and L particles is much weaker than that between the S and M particles and thus require much higher fields for the transition to occur. At slightly higher ferrofluid concentrations (0.4%–0.5%), the interaction between the S and L particles becomes comparable to that between the S and M particles, which allows the field induced transition to occur at smaller field differentials.

Due to the small size of the S particles relative to the M and L particles and its relatively low concentration,

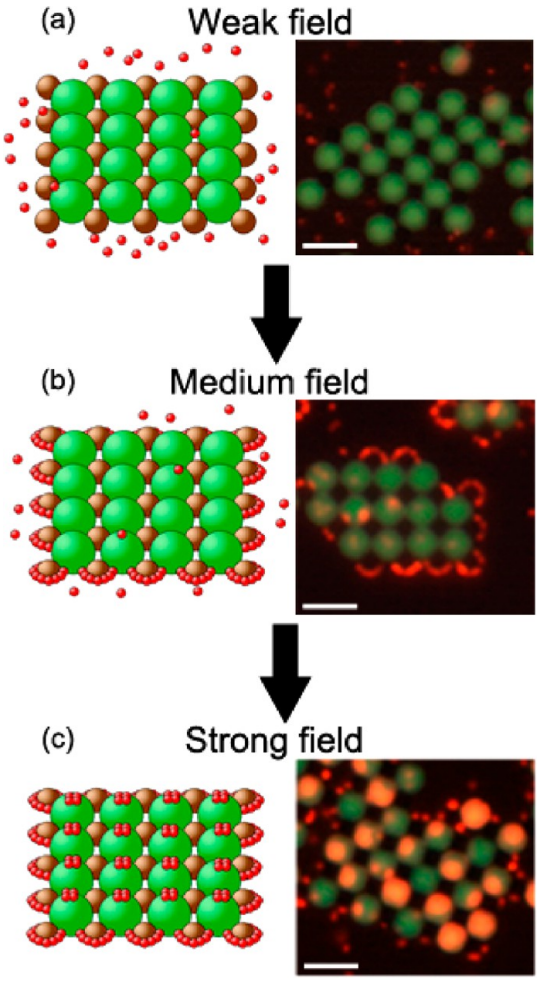

Figure 7. An example of field strength tuned structure transition for the 3-particle system. (a) In a weak field, the structures will only be composed of 4.8 μm nonmagnetic particles and 2.7 μm magnetic particles. (b) In a medium field, the 1 μm particles will form "Saturn Ring" structures with the magnetic particles on the edge of the lattice. (c) In a relatively strong field, in addition to the "Saturn Ring" structures on the edge of the lattice, 1 μm particles can align with 4.8 μm particles and form pole structures. Schematic 3D illustrations are provided for each structure, in which the 1 μm particles (S) are red, 2.7 μm particles (M) are brown, and 4.8 μm particles (L) are green. Scale bar is 10 μm.

its presence does not tend to change the underlying crystal structure; however, its presence does shift the ferrofluid concentrations for which the underlying 2-particle structures are observed. For example, according to the phase diagram in Figure 4, we should not have observed M_4N rings and M_2N chains when the ferrofluid concentration was less than 0.5%, yet these structures were observed in the 3-particle system. It is possible to understand why the S particle introduces a shift in the phase diagram by noting that the effective dipole moment of the composite structure consisting of an M particle surrounded by a ring of S particles is smaller than for an isolated M particle. In a sense, the S particles are playing a similar role as the ferrofluid; that is, for high concentrations of S particles, the effective dipole moments of the M particles can be reduced in a similar manner to increasing the ferrofluid concentration. Likewise, the high concentrations of S particles can increase the effective dipole moments of the L particles by assembling on their poles. Thus, the addition of S particles has the general effect of shifting the range of ferrofluid concentration where a particular structure appears in the phase diagram. This effect only appears when S particles formed composite with M or L particles, which happens above certain field strength. Thus, by adjusting the strength of the external field it may be possible to adjust the crystal structures in real time.

CONCLUSIONS

We present a highly tunable magnetic assembly system which uses ferrofluid to control the interactions between particles of different types and sizes, and we demonstrate a wealth of different structures that can be observed in 2-particle and 3-particle systems. We show that for a 2-particle system, in which the particles are of two different sizes, it is possible to assemble several structures that are not observed in a system of similarly sized particles. Our results also indicate that metastable states can dominate the assembly process in some regimes, leading to the existence of structures that are not the expected from potential energy calculations.

Our experiments in 3-particle systems, in which the smallest particle is significantly smaller than the other two particles and is present at sufficiently low concentrations, show that the small particle does not alter the underlying crystal structure forming between the medium and large particles. However, the small particle can mimic the effect of the ferrofluid by changing the experimental conditions where the underlying 2-particle structures are observed. Furthermore, we demonstrate the ability to adjust the crystal structure in the 3-particle system by changing the external field strength, which is not possible for a 2-particle system. The flexibility both in forming a variety of crystal structures and in tuning the structures in real-time may find applications in the development of smart materials for applications in biosensors[66] and metamaterials.[67,68]

MATERIALS AND METHODS

Materials. The ferrofluid (EMG 707, Ferrotec, Nashua, NH) consists of an aqueous suspension of magnetic nanoparticles having a mean diameter of 10 nm. The stock ferrofluid supplied by the vendor has a volume fraction of 2.0% solids. The 2.7 μm magnetic particles (M-270 Dynabeads, Life Technologies), 4.8 μm green fluorescent nonmagnetic particles (Fluoro-Max G0500, Thermo Scientific), and 1 μm red fluorescent nonmagnetic particles (Fluoro-Max R0100, Thermo Scientific) were obtained from commercial vendors, all having stock concentrations of 1%. The glass slides and coverslips used in the experiments were coated with 10kD silane–polyoxyethylene–carboxylic acid (PG2-CASL-10k, NANOCS, New York, NY), to prevent adhesion between the particles and the substrates.

Particle Mixtures. In experiments, we adjusted the ferrofluid concentration within the range of 0.1% to 1.0% by diluting the ferrofluid with the suspension of magnetic and nonmagnetic particles. Prior to experiments, the particles were concentrated by centrifugation in order to achieve a concentration of 5% by volume fraction in the final suspension. The number ratio of nonmagnetic particles and magnetic particles (N_n/N_m) for the 2-particle system was controlled by changing the relative concentration of the two particle types. For the 3-particle system, we first tested different volume ratios of 1 μm particles, and found that the 3-particle structures formed most reliably when the 1 μm and 2.7 μm particles were suspended at the same volume fraction. If too few 1 μm particles were used, then it led to incomplete rings around the 2.7 μm particles, whereas if too many 1 μm particles were used, then it led to oversaturation of the equator sites around the 2.7 μm particles and competition with the 4.8 μm particles. Because of these considerations, we restricted our experiments to systems where the 1 μm and 2.7 μm particles were suspended at equal volume fractions.

Assembly Apparatus. A 3.5 μL droplet of the colloidal suspension was placed between a glass slide and a coverslip. Mineral oil was used to seal the suspension between a glass slide and coverslip to prevent convection and drying, which makes it possible to extend the experimental time to more than 24 h. A photograph of the sample and experimental setup is shown in Supporting Information, Figure S1. A uniform magnetic field was applied to the fluid cell by passing a constant current through air-core solenoids (Fisher Scientific, Pittsburgh, PA) mounted underneath the sample. The current was controlled by a bipolar operational power amplifier (KEPCO, Flushing, NY) through a Lab VIEW (National Instruments, Austin, TX) program. The external field applied in the 2-particle system ranged from 10 to 15 Oe. In the 3-particle system, we varied the external field in the range of 0–40 Oe in order to observe field induced transitions. A small amount of white noise (~5% current fluctuations) was added to the solenoid. These perturbations, together with thermal fluctuation at room temperature assisted transitions out of metastable states and into lower energy states. In most cases, each assembly was allowed to equilibriate for 4–6 h before taking any images.

In all experiments, an acoustic field was applied to the sample in order to concentrate the particles at local pressure nodes of the acoustic standing wave. The acoustic field was induced by an attached piezoelectric transducer (APC International, Mackeyville, PA) underneath the glass slides. The input to the transducer was a 1 V sine wave at a frequency of 2.932 MHz, which is the resonant frequency of the piezoelectric transducer. After the particles were concentrated in small regions, the

acoustic field was turned off and the magnetic field was turned on to start the magnetic assembly process. A fluorescence microscope with a 40× objective (LEICA, Bannockburn, IL) was used to observe the particle assembly process by taking a combination of bright field and fluorescent images, which were overlaid.

Data Analysis. The particle number ratio was determined using ImagePro (Media Cybernetics). For each image, the predominantly observed structure (over 80% of particles were typically assembled in one type of crystal structure) was plotted in the phase diagram. The dominant phase was identified by observing the relative frequency of appearance of each crystal structure. In cases where multiple crystal phases appear in the experimental system, we split the image into different subimages, and conducted the data analysis on each subimage. Combining all the data from the images and subimages, we plot the most frequent structure (or the most and second most frequent structure if two structures had similar frequency of appearance) in the phase diagram. In cases where two structures were observed at similar frequencies, we separated the data points slightly in the horizontal direction so that both data points can be clearly distinguished. Because the ferrofluid concentration is inferred from the mixing ratio and is not experimentally measured, there is always some ambiguity in the experimental data. Thus, these experiments should be used as an indication for the general conditions for where different crystal structures can be obtained.

Conflict of Interest: The authors declare no competing financial interest.

Acknowledgment. This work is supported by National Science Foundation's Research Triangle Materials Research Science and Engineering Center (DMR-1121107), National Science Foundation of China 51150110161, and the Youth 1000 Scholars Program awarded by the People's Republic of China.

Supporting Information Available: A description of the experimental setup and methods for concentrating the sample with an acoustic field are shown in Figures S1 and S2. Large field of view images of several colloidal phases are shown in Figure S3. The variation of bond angles in 1-D chains as a function of the ferrofluid concentration is shown in Figure S4. Percolating chains networks are shown in Figure S5. A movie of the field induced transition for the 3-particle system is provided, having an elapsed experimental time of 100 min. This material is available free of charge *via* the Internet at http://pubs.acs.org.

REFERENCES AND NOTES

1. Cho, A. Physics: Voila! Cloak of Invisibility Unveiled. *Science* **2006**, *314*, 403–403.
2. Pendry, J. Photonics—Metamaterials in the Sunshine. *Nat. Mater.* **2006**, *5*, 599–600.
3. Liu, N.; Guo, H. C.; Fu, L. W.; Kaiser, S.; Schweizer, H.; Giessen, H. Three-Dimensional Photonic Metamaterials at Optical Frequencies. *Nat. Mater.* **2008**, *7*, 31–37.
4. Soukoulis, C. M.; Wegener, M. Past Achievements and Future Challenges in the Development of Three-Dimensional Photonic Metamaterials. *Nat. Photonics* **2011**, *5*, 523–530.
5. Mary, A.; Rodrigo, S. G.; Garcia-Vidal, F. J.; Martin-Moreno, L. Theory of Negative-Refractive-Index Response of Double-Fishnet Structures. *Phys. Rev. Lett.* **2008**, *101*, 103902.
6. Kuo, N. K.; Piazza, G. Fractal Phononic Crystals in Aluminum Nitride: An Approach to Ultra High Frequency Bandgaps. *Appl. Phys. Lett.* **2011**, *99*, 163501.
7. Cheng, W.; Wang, J. J.; Jonas, U.; Fytas, G.; Stefanou, N. Observation and Tuning of Hypersonic Bandgaps in Colloidal Crystals. *Nat. Mater.* **2006**, *5*, 830–836.
8. Cao, L. S.; Peng, R. W.; Zhang, R. L.; Zhang, X. F.; Wang, M.; Huang, X. Q.; Hu, A.; Jiang, S. S. Delocalization of Phonons and Quantized Thermal Conductance in a Random *n*-Mer System. *Phys. Rev. B* **2005**, *72*, 214301.
9. Liu, R.; Ji, C.; Mock, J. J.; Chin, J. Y.; Cui, T. J.; Smith, D. R. Broadband Ground-Plane Cloak. *Science* **2009**, *323*, 366–369.
10. Cheng, Y.; Liu, X. J. Specific Multiple-Scattering Process in Acoustic Cloak with Multilayered Homogeneous Isotropic Materials. *J. Appl. Phys.* **2008**, *104*, 104911.
11. Gomory, F.; Solovyov, M.; Souc, J.; Navau, C.; Prat-Camps, J.; Sanchez, A. Experimental Realization of a Magnetic Cloak. *Science* **2012**, *335*, 1466–1468.
12. Lu, C. C.; Hu, X. Y.; Yang, H.; Gong, Q. H. Ultrahigh-Contrast and Wideband Nanoscale Photonic Crystal All-Optical Diode. *Opt. Lett.* **2011**, *36*, 4668–4670.
13. Fan, Y. C.; Han, J.; Wei, Z. Y.; Wu, C.; Cao, Y.; Yu, X.; Li, H. Q. Subwavelength Electromagnetic Diode: One-Way Response of Cascading Nonlinear Meta-Atoms. *Appl. Phys. Lett.* **2011**, *98*, 151903.
14. Li, B. W.; Wang, L.; Casati, G. Thermal Diode: Rectification of Heat Flux. *Phys. Rev. Lett.* **2004**, *93*, 184301.
15. Yang, L. Finite Heat Conduction in a 2D Disorder Lattice. *Phys. Rev. Lett.* **2002**, *88*, 119401.
16. Liang, B.; Yuan, B.; Cheng, J. C. Acoustic Diode: Rectification of Acoustic Energy Flux in One-Dimensional Systems. *Phys. Rev. Lett.* **2009**, *103*, 104301.
17. Li, X. F.; Ni, X.; Feng, L. A.; Lu, M. H.; He, C.; Chen, Y. F. Tunable Unidirectional Sound Propagation through a Sonic-Crystal-Based Acoustic Diode. *Phys. Rev. Lett.* **2011**, *106*, 084301.
18. Pendry, J. B.; Schurig, D.; Smith, D. R. Controlling Electromagnetic Fields. *Science* **2006**, *312*, 1780–1782.
19. Martin, F.; Ziolkowski, R. Microwave Metamaterials: Application to Devices, Circuits and Antennas. *IET Microwaves Antennas Propagat.* **2010**, *4*, 975–976.
20. Lam, V. D.; Kim, J. B.; Lee, S. J.; Lee, Y. P. Left-Handed Behavior of Combined and Fishnet Structures. *J. Appl. Phys.* **2008**, *103*, 033107.
21. Bogaerts, W.; Wiaux, V.; Taillaert, D.; Beckx, S.; Luyssaert, B.; Bienstman, P.; Baets, R. Fabrication of Photonic Crystals in Silicon-On-Insulator Using 248-nm Deep UV Lithography. *IEEE J. Sel. Top. Quant.* **2002**, *8*, 928–934.
22. Jiang, L. Y.; Jia, W.; Zheng, G. G.; Li, X. Y. Design and Fabrication of Rod-Type Two-Dimensional Photonic Crystal Slabs with Large High-Order Bandgaps in Near-Infrared Wavelengths. *Opt. Lett.* **2012**, *37*, 1424–1426.
23. Garcia-Pomar, J. L.; Gollub, J. N.; Mock, J. J.; Smith, D. R.; Nieto-Vesperinas, M. Experimental Two-Dimensional Field Mapping of Total Internal Reflection Lateral Beam Shift in a Self-Collimated Photonic Crystal. *Appl. Phys. Lett.* **2009**, *94*, 061121.
24. Bita, I.; Choi, T.; Walsh, M. E.; Smith, H. L.; Thomas, E. L. Large-Area 3D Nanostructures with Octagonal Quasicrystalline Symmetry *via* Phase-Mask Lithography. *Adv. Mater.* **2007**, *19*, 1403–1407.
25. Jang, J. H.; Ullal, C. K.; Maldovan, M.; Gorishnyy, T.; Kooi, S.; Koh, C. Y.; Thomas, E. L. 3D Micro- and Nanostructures *via* Interference Lithography. *Adv. Funct. Mater.* **2007**, *17*, 3027–3041.
26. Boncheva, M.; Whitesides, G. M. Making Things by Self-Assembly. *MRS Bull.* **2005**, *30*, 736–742.
27. Bowden, N.; Terfort, A.; Carbeck, J.; Whitesides, G. M. Self-Assembly of Mesoscale Objects into Ordered Two-Dimensional Arrays. *Science* **1997**, *276*, 233–235.
28. Grill, L.; Dyer, M.; Lafferentz, L.; Persson, M.; Peters, M. V.; Hecht, S. Nano-Architectures by Covalent Assembly of Molecular Building Blocks. *Nat. Nanotechnol* **2007**, *2*, 687–691.
29. Mann, S. Self-Assembly and Transformation of Hybrid Nano-objects and Nanostructures under Equilibrium and Non-equilibrium Conditions. *Nat. Mater.* **2009**, *8*, 781–792.
30. Zerrouki, D.; Baudry, J.; Pine, D.; Chaikin, P.; Bibette, J. Chiral Colloidal Clusters. *Nature* **2008**, *455*, 380–382.
31. Chang, C. H.; Tian, L.; Hesse, W. R.; Gao, H.; Choi, H. J.; Kim, J. G.; Siddiqui, M.; Barbastathis, G. From Two-Dimensional Colloidal Self-Assembly to Three-Dimensional Nanolithography. *Nano Lett.* **2011**, *11*, 2533–2537.
32. Xia, Y. N.; Gates, B.; Li, Z. Y. Self-Assembly Approaches to Three-Dimensional Photonic Crystals. *Adv. Mater.* **2001**, *13*, 409–413.

33. Bhawalkar, S. P.; Qian, J.; Heiber, M. C.; Jia, L. Development of a Colloidal Lithography Method for Patterning Nonplanar Surfaces. *Langmuir* **2010**, *26*, 16662–16666.
34. Chung, J. H.; Zheng, W.; Hatch, T. J.; Jacobs, H. O. Programmable Reconfigurable Self-Assembly: Parallel Heterogeneous Integration of Chip-Scale Somponents on Planar and Nonplanar Surfaces. *J. Microelectromech. Syst.* **2006**, *15*, 457–464.
35. Rabani, E.; Reichman, D. R.; Geissler, P. L.; Brus, L. E. Drying-Mediated Self-Assembly of Nanoparticles. *Nature* **2003**, *426*, 271–274.
36. Masuda, Y.; Tomimoto, K.; Koumoto, K. Two-dimensional Self-Assembly of Spherical Particles Using a Liquid Mold and its Drying Process. *Langmuir* **2003**, *19*, 5179–5183.
37. Sen, D.; Mazumder, S.; Melo, J. S.; Khan, A.; Bhattyacharya, S.; D'Souza, S. F. Evaporation Driven Self-Assembly of a Colloidal Dispersion during Spray Drying: Volume Fraction Dependent Morphological Transition. *Langmuir* **2009**, *25*, 6690–6695.
38. Yethiraj, A.; van Blaaderen, A. A Colloidal Model System with an Interaction Tunable from Hard Sphere to Soft and Dipolar. *Nature* **2003**, *421*, 513–519.
39. Leunissen, M. E.; Christova, C. G.; Hynninen, A. P.; Royall, C. P.; Campbell, A. I.; Imhof, A.; Dijkstra, M.; van Roij, R.; van Blaaderen, A. Ionic Colloidal Crystals of Oppositely Charged Particles. *Nature* **2005**, *437*, 235–240.
40. Kalsin, A. M.; Kowalczyk, B.; Smoukov, S. K.; Klajn, R.; Grzybowski, B. A. Ionic-like Behavior of Oppositely Charged Nanoparticles. *J. Am. Chem. Soc.* **2006**, *128*, 15046–15047.
41. Braun, E.; Eichen, Y.; Sivan, U.; Ben-Yoseph, G. DNA-Templated Assembly and Electrode Attachment of a Conducting Silver Wire. *Nature* **1998**, *391*, 775–778.
42. Shyr, M. H.; Wernette, D. P.; Wiltzius, P.; Lu, Y.; Braun, P. V. DNA and DNAzyme-Mediated 2D Colloidal Assembly. *J. Am. Chem. Soc.* **2008**, *130*, 8234–8240.
43. Valignat, M. P.; Theodoly, O.; Crocker, J. C.; Russel, W. B.; Chaikin, P. M. Reversible Self-Assembly and Directed Assembly of DNA-Linked Micrometer-Sized Colloids. *Proc. Natl. Acad. Sci. U.S.A.* **2005**, *102*, 4225–4229.
44. Nykypanchuk, D.; Maye, M. M.; van der Lelie, D.; Gang, O. DNA-Guided Crystallization of Colloidal Nanoparticles. *Nature* **2008**, *451*, 549–552.
45. Kim, A. J.; Biancaniello, P. L.; Crocker, J. C. Engineering DNA-Mediated Colloidal Crystallization. *Langmuir* **2006**, *22*, 1991–2001.
46. Ristenpart, W. D.; Aksay, I. A.; Saville, D. A. Electrically Guided Assembly of Planar Superlattices in Binary Colloidal Suspensions. *Phys. Rev. Lett.* **2003**, *90*, 128303.
47. Erb, R. M.; Son, H. S.; Samanta, B.; Rotello, V. M.; Yellen, B. B. Magnetic Assembly of Colloidal Superstructures with Multipole Symmetry. *Nature* **2009**, *457*, 999–1002.
48. Khalil, K. S.; Sagastegui, A.; Li, Y.; Tahir, M. A.; Socolar, J. E.; Wiley, B. J.; Yellen, B. B. Binary Colloidal Structures Assembled through Ising Interactions. *Nat. Commun* **2012**, *3*, 794.
49. Sacanna, S.; Irvine, W. T.; Chaikin, P. M.; Pine, D. J. Lock and Key Colloids. *Nature* **2010**, *464*, 575–578.
50. Wang, R. M.; Li, P. W.; Chen, C. P. Template-free Synthesis and Self-Assembly of Aligned Nickel Nanochains under Magnetic Fields. *J. Nanosci. Nanotechnol.* **2011**, *11*, 11128–11132.
51. Fang, W. X.; He, Z. H.; Xu, X. Q.; Mao, Z. Q.; Shen, H. Magnetic-Field-Induced Chain-like Assembly Structures of Fe_3O_4 Nanoparticles. *Europhys. Lett.* **2007**, *7*, 68004.
52. Velev, O. D.; Bhatt, K. H. On-Chip Micromanipulation and Assembly of Colloidal Particles by Electric Fields. *Soft Matter* **2006**, *2*, 738–750.
53. Yeh, S. R.; Seul, M.; Shraiman, B. I. Assembly of Ordered Colloidal Aggregates by Electric-Field-Induced Fluid Flow. *Nature* **1997**, *386*, 57–59.
54. Ryan, K. M.; Mastroianni, A.; Stancil, K. A.; Liu, H. T.; Alivisatos, A. P. Electric-Field-Assisted Assembly of Perpendicularly Oriented Nanorod Superlattices. *Nano Lett.* **2006**, *6*, 1479–1482.
55. He, L.; Hu, Y. X.; Kim, H.; Ge, J. P.; Kwon, S.; Yin, Y. D. Magnetic Assembly of Nonmagnetic Particles into Photonic Crystal Structures. *Nano Lett.* **2010**, *10*, 4708–4714.
56. Mirica, K. A.; Ilievski, F.; Ellerbee, A. K.; Shevkoplyas, S. S.; Whitesides, G. M. Using Magnetic Levitation for Three Dimensional Self-Assembly. *Adv. Mater.* **2011**, *23*, 4134–4140.
57. Yellen, B. R.; Friedman, G. Programmable Assembly of Heterogeneous Colloidal Particle Arrays. *Adv. Mater.* **2004**, *16*, 111–115.
58. He, L.; Wang, M. S.; Ge, J. P.; Yin, Y. D. Magnetic Assembly Route to Colloidal Responsive Photonic Nanostructures. *Acc. Chem. Res.* **2012**, *45*, 1431–1440.
59. Krebs, M. D.; Erb, R. M.; Yellen, B. B.; Samanta, B.; Bajaj, A.; Rotello, V. M.; Alsberg, E. Formation of Ordered Cellular Structures in Suspension *via* Label-free Negative Magnetophoresis. *Nano Lett.* **2009**, *9*, 1812–1817.
60. Frenkel, D. Entropy-Driven Phase Transitions. *Phys. A* **1999**, *263*, 26–38.
61. Haji-Akbari, A.; Engel, M.; Keys, A. S.; Zheng, X. Y.; Petschek, R. G.; Palffy-Muhoray, P.; Glotzer, S. C. Disordered, Quasicrystalline and Crystalline Phases of Densely Packed Tetrahedra. *Nature* **2009**, *462*, 773–777.
62. Granfeldt, M. K.; Jonsson, B.; Woodward, C. E. A Monte-Carlo Simulation Study of the Interaction between Charged Colloids Carrying Adsorbed Polyelectrolytes. *J. Phys. Chem.* **1991**, *95*, 4819–4826.
63. Zhang, K.; Charbonneau, P. [N]pT Ensemble and Finite-Size-Scaling Study of the Critical Isostructural Transition in the Generalized Exponential Model of Index 4. *Phys. Rev. E* **2012**, *86*, 042501.
64. Goyal, A.; Hall, C. K.; Velev, O. D. Self-Assembly in Binary Mixtures of Dipolar Colloids: Molecular Dynamics Simulations. *J. Chem. Phys.* **2010**, *133*, 064511.
65. Holm, E. A.; Foiles, S. M. How Grain Growth Stops: A Mechanism for Grain-Growth Stagnation in Pure Materials. *Science* **2010**, *328*, 1138–1141.
66. Yang, Y.; Morimoto, Y.; Takamura, T.; Sandhu, A. Biosensing Based on Magnetically Induced Self-Assembly of Particles in Magnetic Colloids. *J. Nanosci. Nanotechnol.* **2012**, *12*, 2081–2088.
67. Fafarman, A. T.; Hong, S. H.; Caglayan, H.; Ye, X.; Diroll, B. T.; Paik, T.; Engheta, N.; Murray, C. B.; Kagan, C. R., Chemically Tailored Dielectric-to-Metal Transition for the Design of Metamaterials from Nanoimprinted Colloidal Nanocrystals. *Nano Lett.* **2012**, Article ASAP.
68. Alu, A.; Engheta, N. Cloaking and Transparency for Collections of Particles with Metamaterial and Plasmonic Covers. *Opt. Express* **2007**, *15*, 7578–7590.